Negative-positive oscillation in interfacial friction of a In_2Se_3-graphene heterojunction

Jiangtao Cheng, Kun Liu, Xingju Zhao, Xinlian Xue,* Lili Zhang, Rui Pang, Xiaoyan Ren,† and Shunfang Li‡

Key Laboratory of Material Physics, Ministry of Education, School of Physics and Microelectronics, Zhengzhou University, Zhengzhou 450001, China

(Received 18 June 2022; revised 2 November 2022; accepted 8 November 2022; published 17 November 2022)

According to the classic law of Da Vinci-Amontons, a friction force f was found to increase macroscopically with an external normal load $N(f = \mu N)$, with a positive definite friction coefficient μ. Here we employ first-principles calculations to predict that, when sliding the ferroelectric two-dimensional In_2Se_3 over graphene, the differential friction coefficient μ, measured by the slope of the corrugation in the sliding potential energy barrier subject to load N, displays an overall positive feather when the dipole is aligned toward the In_2Se_3-graphene interface; however, μ exhibits intriguing negative-positive oscillation with increasing N when the dipole is aligned outward from the interface. Such striking observations can be rationalized by the van der Waals and electrostatic interaction-induced competition between the downward shift of the sliding barrier by the p_x- and p_y-like levels and the upward shift of the barrier by the p_z states, which is accompanied by an oscillation of the In_2Se_3-graphene interfacial charge redistribution subject to the external load. The present findings are expected to play an instrumental role in the design of high-performance solid lubricants.

DOI: 10.1103/PhysRevB.106.195416

I. INTRODUCTION

Friction, one of the oldest and most important phenomena due to its enormous practical and technological importance, has stimulated continued progress over the centuries [1,2]. Actually, friction has two sides when it comes to practical applications: Sometimes it is exploited to improve our lives [3,4], but in most cases reduced friction is desirable to save mechanical energy dissipation and surface wear [5,6]. It was estimated that about one-third to one-half of the world's primary energy is dissipated in mechanical friction [7,8], and 80% of machinery component failure is caused by wear [9]. Moreover, friction may play an instrumental role in diverse systems—from macroscopic equipment [10–12], to nanometer contacts in nanomachines [2,13,14], to biological molecular motors [15,16]. In particular, with the development of nanoscience and nanotechnology, understanding and controlling friction in the nanometer regime is of great significance when designing highly efficient micro- and nanoelectromechanical systems, especially for situations in which *tunable* friction is required to determine the efficiency and lifetime of these nanodevices [17]. Correspondingly, developing high-quality lubricants that result in even a modest reduction of friction can substantially contribute to energy savings in running nanodevices/nanomachines and reduce carbon dioxide emission [8].

At the nanometer-scale regime, friction can exhibit distinct behaviors from those at the macroscopic scale. In the latter case, according to Da Vinci-Amontons law ($f = \mu N$), friction force f increases with increasing normal load N with a positive definite friction coefficient μ, and the friction force f is independent of other factors, such as contact area, sliding velocity, etc. However, such a classic law has been demonstrated to break down at the microscopic regime by extensive observations that friction becomes sensitive to various factors such as temperature [18,19], sliding velocity [20–22], size/thickness effects [23–25], and surface roughness [26,27]. These findings offer a promising avenue toward microscopic understanding and modulating friction.

Various approaches have been developed to reduce and control friction, such as changing the sliding contact by modifying surface roughness or adding lubricants. Among them, the concept of structural superlubricity is considered one of the most effective methods to achieve extremely low friction [12,28] when two crystalline surfaces slide over each other in dry incommensurate contact without wear and deformation. In contrast to liquid lubrications, which may fail in some extreme conditions [29,30], structural superlubricity essentially originated from the effective cancelation of lateral forces within incommensurate rigid crystalline contacts, and thus significantly reduced the sliding energy barriers to the motion [31–33]. More intriguingly, adhesion-dependent negative friction coefficients of chemically modified graphite have been recently reported [34,35]. Note that, here, the negative friction coefficient could be more rigorously expressed as negative differential friction (NDF) [36,37], coined by analogy to another very popular concept of negative differential resistance [38,39]. Moreover, NDF was also theoretically/experimentally probed in superlubric two-dimensional (2D) graphene-hexagonal boron nitride heterojunctions [40], graphene-graphene [41], and ferroelectric

*xuexinlian@zzu.edu.cn
†renxyan@zzu.edu.cn
‡sflizzu@zzu.edu.cn

materials [33], which were sustained either by the condition of incommensurate contacts, which may be blocked to commensurate configurations during the sliding or by the reduction of the potential corrugation by the van der Waals (vdW) interactions in the attractive regime of the interfacial separation above its equilibrium [42,43]. In addition, stick–slip and other "anomalies" in friction on suspended and supported graphene due to local deformation and thermal effects have also been reported [44–47].

Here, we propose that, as a unique member of the 2D material family, 2D ferroelectric material may offer new opportunities to tune the tribological properties due to its tunable polarization under external load [48], which is absent in other types of sliding 2D contacts. Very recently, our group predicted a negative differential friction coefficient μ when sliding one quintuple layer (1QL) of ferroelectric In_2Se_3 over another commensurate QL-In_2Se_3 [49], which can be rationalized by the delicate interplay of the interfacial van der Waals repulsive interactions and the dipole–dipole alignment-dependent electrostatic energy reduction. As a new finding, taking the In_2Se_3-graphene heterostructure as a typical incommensurate contact, we employ first-principles calculations to demonstrate that the differential friction coefficient μ, measured by the slope of the corrugation in the sliding potential energy barrier subject to an external load N, can be readily tuned by the electric polarization direction of the 2D In_2Se_3 polar material. That is, positive μ is observed when the dipole is aligned toward the In_2Se_3-graphene interface, however, μ exhibits an intriguing negative-positive oscillation as a function of applied normal load N when the dipole is aligned outward from the interface. That is, μ can be tuned to be either negative or positive, depending on the external load regime and dipole alignments. Such striking observations can be rationalized by the vdW interaction-induced competition between the downward shift of the relatively low-energy p_x- and p_y-like levels, and the upward shift of the high-energy p_z states, which are accompanied by an oscillation of the In_2Se_3-graphene interfacial charge redistribution subject to the external load.

II. METHODS

The calculations were carried out using density functional theory (DFT) [50] as implemented in VASP code [51]. The interactions of valence electrons with atomic cores were described by the projector-augmented wave method [52], as parameterized by the Perdew–Burke–Ernzerhof functional [53]. We adopted the zero damping DFT-D3 of Grimme method [54] to describe correctly both the ground-state phase of 1QL-In_2Se_3 and the vdW interactions of the present graphene-In_2Se_3 heterostructure in consideration of dipole corrections versus comparisons with other schemes (e.g., many-body dispersion vdW model), as suggested in previous work [49]. Moreover, we reexamined the relative stability of the 1QL-In_2Se_3 between the α and β phases, and confirmed that the α configuration is the ground state [55]. Note that a constant external load is exerted on the surface atoms of the topmost 1QL-In_2Se_3 layer in the z direction with modified code by the introduction of an extra force on the calculated Hellmann–Feynman force in the Kohn–Sham equation, which was rigorously examined during our previous investigation [49]. In our calculations, the electronic wave functions are expanded in a plane-wave basis, with an energy cutoff of 500 eV. To limit the lattice mismatch between α-In_2Se_3 ($a = 4.11$ Å) and graphene ($a = 2.46$ Å), a 3×3 α-In_2Se_3 is used to match a 5×5 graphene in our simulation supercell, with a vacuum region of more than 15 Å, resulting in a merely biaxial compressive strain of 0.15% for 1QL-In_2Se_3. A saw-like self-consistent dipole layer was placed in the middle of the vacuum region to adjust the misalignment between the vacuum levels on the different sides of the film due to the intrinsic electric polarization. A Γ-centered $9 \times 9 \times 1$ Monkhorst–Pack k-mesh was used for k-point sampling to converge the total energy within 10^{-5} eV.

III. RESULTS AND DISCUSSION

First, we examined the lattice constants of In_2Se_3 and graphene, which are 4.11 and 2.46 Å, respectively, in close agreement with experimental/calculations [55–57]. Due to the significantly different interlayer spacing between the selenium layer and the two indium layers and the in-plane centrosymmetry breaking, the optimized 1QL-In_2Se_3 per unit cell results in spontaneous out-of-plane (∼0.1 eÅ) and in-plane (∼2.4 eÅ) electric polarizations, respectively, which is also in close agreement with previous calculations [55] and experimental observations [58,59]. As shown in Fig. 1(a), the 1QL-In_2Se_3 has two distinct surfaces in contact with graphene, with the ferroelectric polarization either pointing upward (P ↑) or downward (P ↓), respectively. Correspondingly, in the case of P ↑, the surface in contact with the underlying graphene is termed down-surface (DS) and the other surface is named up-surface (US). Moreover, as also schematically highlighted, the In_2Se_3 overlayer can be divided into two subunits—$InSe_2$ and InSe—that accommodate the negative and positive charge center of the ferroelectric In_2Se_3 structure, respectively.

Our calculations show that the P ↑ In_2Se_3-graphene contact (hereafter termed P ↑) is slightly more stable than P ↓ In_2Se_3-graphene (P ↓), as manifested by the calculated interlayer binding energies of 2.076 and 1.918 eV for the former and latter, respectively, in close agreement with previous calculations [60]. Such a difference can be addressed from the distinct work functions (WFs) between graphene and In_2Se_3. The calculated WF of the freestanding graphene is 4.22 eV, which is smaller than that of both the DS and US of the In_2Se_3 monolayer by 1.76 and 0.66 eV, respectively.

Therefore, in the case of the P ↑ contact, relative to the case of P ↓, more electrons can be transferred from graphene to In_2Se_3, enhancing the interfacial binding of the former. Bader charge analysis demonstrates a net charge (0.004 $|e|$/C atom) tunneled from the graphene to the In_2Se_3 overlayer in the P ↑ contact; however, a negligible charge transfer is identified in the case of P ↓, as also demonstrated by the charge and band structure analysis shown in Fig. 1(b)–1(d). Note that the charge transfer from graphene to In_2Se_3 around the interface of the P ↑ contact results in an induced dipole, which is antiparallel to the intrinsic dipole of the In_2Se_3 overlayer. Therefore, the repulsive interaction of the induced and intrin-

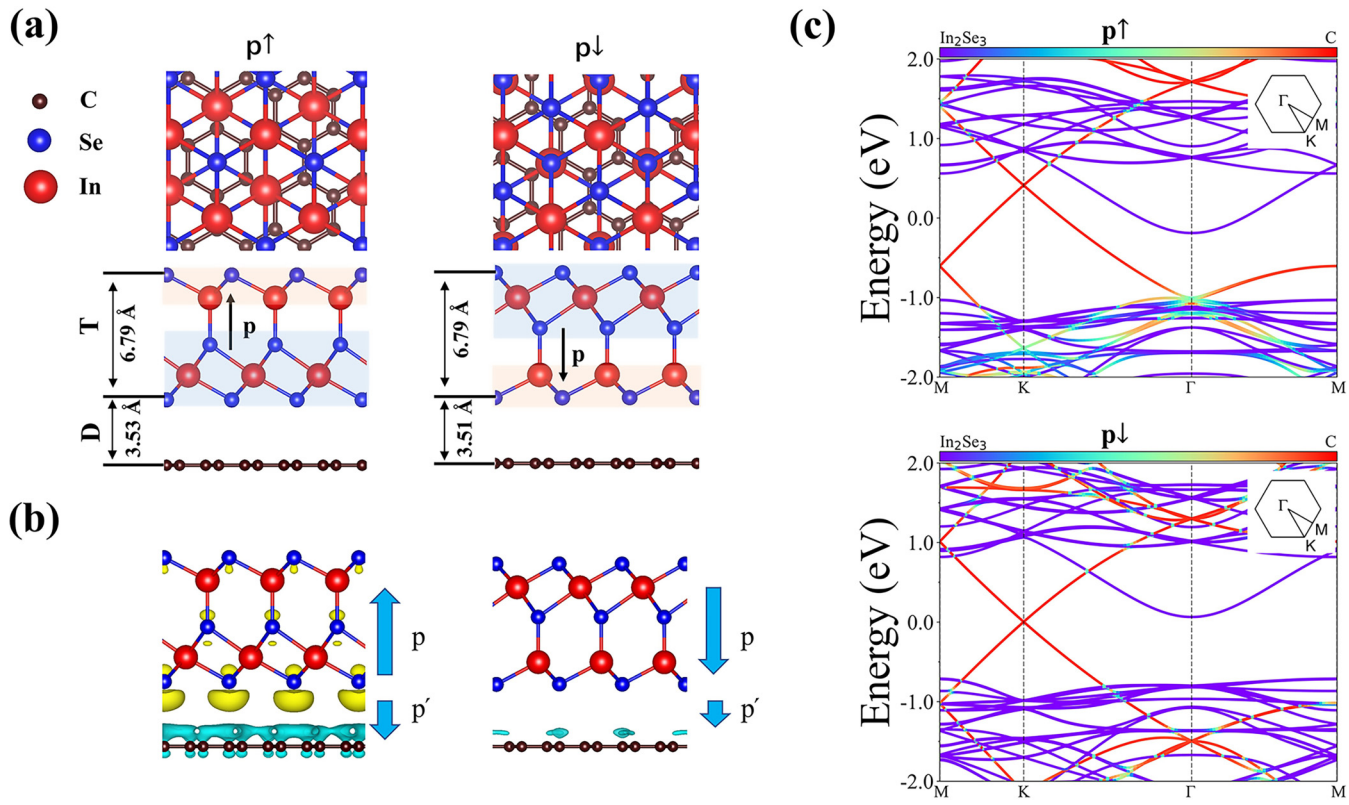

FIG. 1. Schematic illustrations of the geometric and electronic structures of the In_2Se_3-graphene heterojunction. (a) Top and side views of two typical contacts for the quintuple layers (1QL) In_2Se_3 on graphene (In_2Se_3-graphene), with the ferroelectric polarization either pointing upward (P ↑) or downward (P ↓). (b) Side views of the charge transfer between In_2Se_3 and graphene. Yellow and blue denote charge accumulation and depletion, respectively. The first Brillouin zone and decomposed electronic band structures of the two types of In_2Se_3-graphene heterojunctions: (c) P ↑ and (d) P ↓ .

sic dipoles in the P ↑ contact results in a slightly enlarged interfacial separation by 0.04 Å compared to 2.51 Å in P ↓, which is also in line with previous calculations [60].

Next, we introduced our simulation model in investigating the friction behaviors of these two contacts under external loads. As schematically shown in Fig. 2(a), when sliding 1QL-In_2Se_3 over graphene, external forces are applied to the topmost atoms of the 1QL-In_2Se_3 overlayer. Moreover, the bottom 2D graphene keeps almost exactly flat under the pressure of the 2D In_2Se_3, rather than leading to significant local deformation by the probing tip, as observed in experiments [23,24]. Therefore, in our simulations, all the atoms of the bottom graphene are fixed to the equilibrium position of the freestanding honeycomb structure. When sliding the 1QL-In_2Se_3 over the graphene substrate, the x, y, and z coordinates of the atoms in graphene are fully fixed, and the energy profile of the 1QL-In_2Se_3-graphene contact is optimized by displacing the top 1QL-In_2Se_3 every 0.205 Å [32] along the proposed directions, with fixing the x and y coordinates of the top-two layers of atoms. That is, when quasi-statically sliding the 1QL-In_2Se_3 overlayer along both [110] and [100] pathways in a periodic unit, 20 points with identical distances are adopted, following with optimizations, to obtain the sliding energy profiles. In this process, the z coordinates of the top-two layers and the x, y, and z coordinates of the bottom-three atomic layers of 1QL-In_2Se_3 can be fully relaxed under an external load.

Now we define the friction force in the sliding processes. First, as shown in Fig. 2(b), we present the energy profile of 1QL-In_2Se_3 displacing on the graphene substrate along [110] without load. One can see that, starting from the lowest energy minimum (E_{min}) configuration based on extensive geometric staking searching, during one sliding period, several local maxima of energy are identified, with the highest energy maximum (E_{max}) occurring when the interfacial selenium atoms are slid around to the top site of the underlying C atom. Then, we define the load-dependent sliding energy barriers E_{bar} as $E_{bar} = E_{max}–E_{min}$. Dividing E_{bar} by the sliding distance, we can estimate the friction force f.

We further investigate E_{bar} and the differential friction coefficient ($\mu = df/dN$) for both the P ↑ and P ↓ In_2Se_3-graphene contacts as a function of external load. Distinct relationships between E_{bar} and the load for P ↑ and P ↓ can be seen in Fig. 2(c). Specifically, for the case of P ↑, in the load regime of $N = 0.0$ to 1.1 GPa, the calculated E_{bar} monotonously increases, corresponding to a definite positive differential friction coefficient μ, i.e., $\mu > 0$, as shown by the dashed line in Fig. 2(c). However, in the range of $N = 1.10$ to 1.65 GPa, E_{bar} decreases as the load increases, leading to negative μ, i.e., $\mu < 0$. Intriguingly, as the external load further increases, E_{bar} exhibits significant positive-negative oscillations as a function of the external load, i.e., we obtain $\mu > 0$ in the load regimes of $N = 1.65$ to 2.20 and 2.75 to 3.30 GPa, and $\mu < 0$ within the load ranges of $N = 1.10$ to

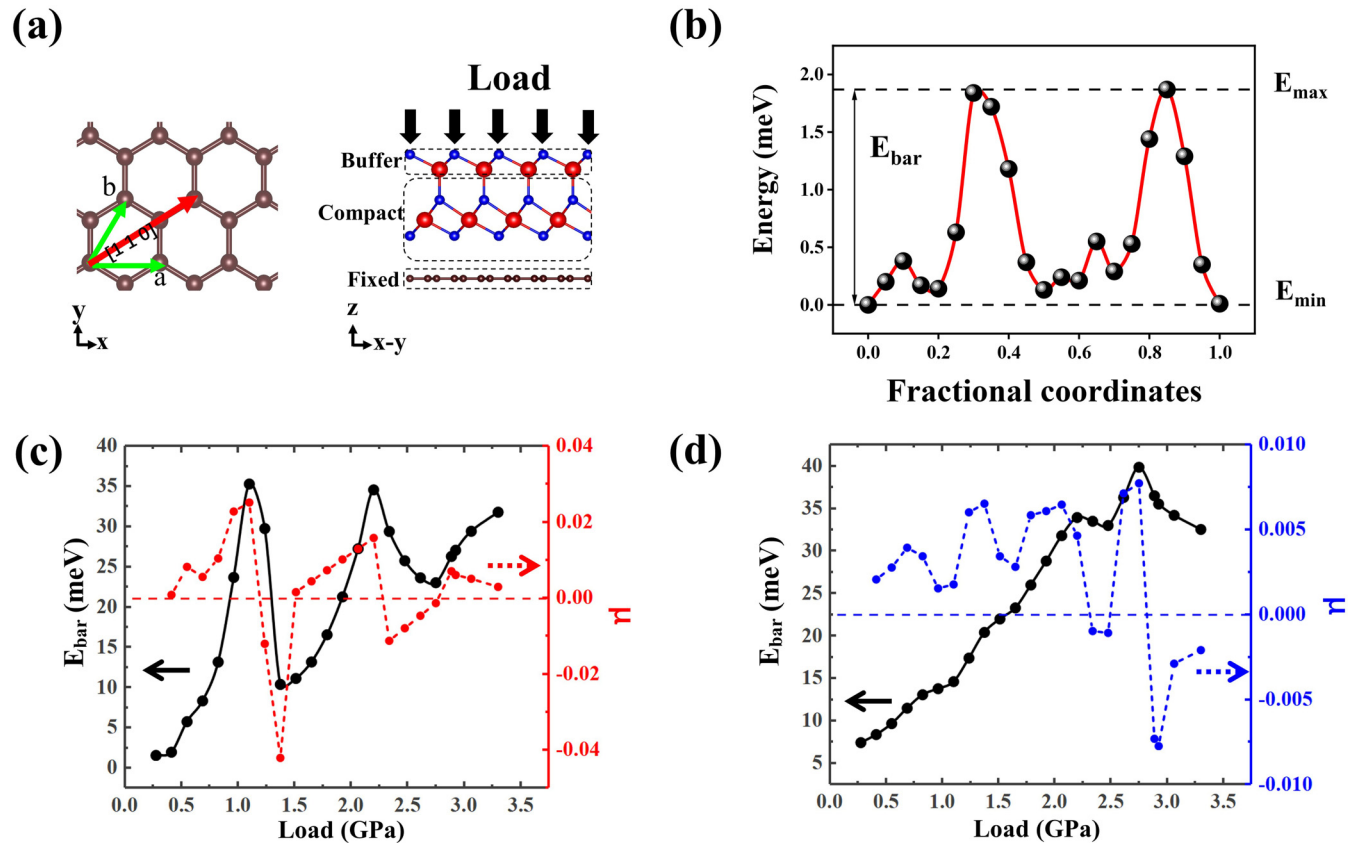

FIG. 2. Frictional properties of 1QL-In_2Se_3 over graphene. (a) Schematic representation of the model in simulations of sliding P ↑ 1QL-In_2Se_3 over graphene (P ↑). Two sliding pathways along [110] and [100] are marked. (b) Sliding energy profile of the P ↑ 1QL-In_2Se_3 over graphene along [110] without external load. (c) and (d) Load-dependent sliding energy barriers (E_{bar}) and differential friction coefficient ($\mu = df/dN$) along the [110] pathway for both the P ↑ and the P ↓ 1QL-In_2Se_3-graphene contact.

1.65 and 2.20 to 2.75 GPa, respectively. That is, the oscillation period is about 0.55 GPa. Note that, taking the calculated E_{bar} at both 0.0 and 1.1 GPa as representative cases, we have also considered the finite temperature effect (entropy) and zero-point energy correction to E_{bar}. Our calculations show that the zero-point energy and entropy corrections at room temperature are negligible, merely around several millielectron volts, which cannot disturb the oscillation feature of the E_{bar} profile. However, as seen from Fig. 2(d), for P ↓, the overall E_{bar} begins to drop as the load increases up to around 2.75 GPa, corresponding to the feature of a positive-to-negative transition of the friction coefficient μ.

To rationalize these findings to the first-order of approximation, we decompose the calculated E_{bar} into different terms that can be contributed separately by interfacial and intralayer interactions. For the present In_2Se_3-graphene heterostructure, the bottom 2D graphene becomes almost exactly flat under pressure; therefore, in our simulations, all the atoms of the bottom graphene are totally fixed to the equilibrium position of the freestanding 2D structure. Therefore, when sliding the In_2Se_3 overlayer under external pressure, both the thickness of 1QL-In_2Se_3 and the interfacial distance between In_2Se_3 and the underlying graphene will be reduced, which contributes to the energy cost and thus the friction [49], as manifested by the change of the sliding potential energy profile. According to our simulation model, the sliding E_{bar} can be defined as

$$E_{bar} = E_{max}(In_2Se_3 - \text{graphene}) - E_{min}(In_2Se_3 - \text{graphene}). \quad (1)$$

Qualitatively, E_{bar} can be divided into two parts:

$$E_{bar} = E_{bar-inter} + E_{bar-def}. \quad (2)$$

More specifically, the first term on the right-hand side of Eq. (2) can be expressed as

$$\begin{aligned} E_{bar-inter} = &[E_{max}(In_2Se_3 - \text{graphene}) - E_{max}(In_2Se_3) \\ &- E_{max}(\text{graphene})] - [E_{min}(In_2Se_3 - \text{graphene}) \\ &- E_{min}(In_2Se_3) - E_{min}(\text{graphene})], \end{aligned} \quad (3)$$

where the six terms on the right-hand side of the equation represent the energy maximum and minimum states of the 1QL-In_2Se_3-graphene complex, and the In_2Se_3 and graphene components, respectively.

Based on these definitions, E_{bar} originating from the deformation of the In_2Se_3 overlayer from its equilibrium state (E_0) in the gas phase can be deduced:

$$\begin{aligned} E_{bar-def} &= [E_{max}(In_2Se_3) - E_0] - [E_{min}(In_2Se_3) - E_0] \\ &= E_{max}(In_2Se_3) - E_{min}(In_2Se_3). \end{aligned} \quad (4)$$

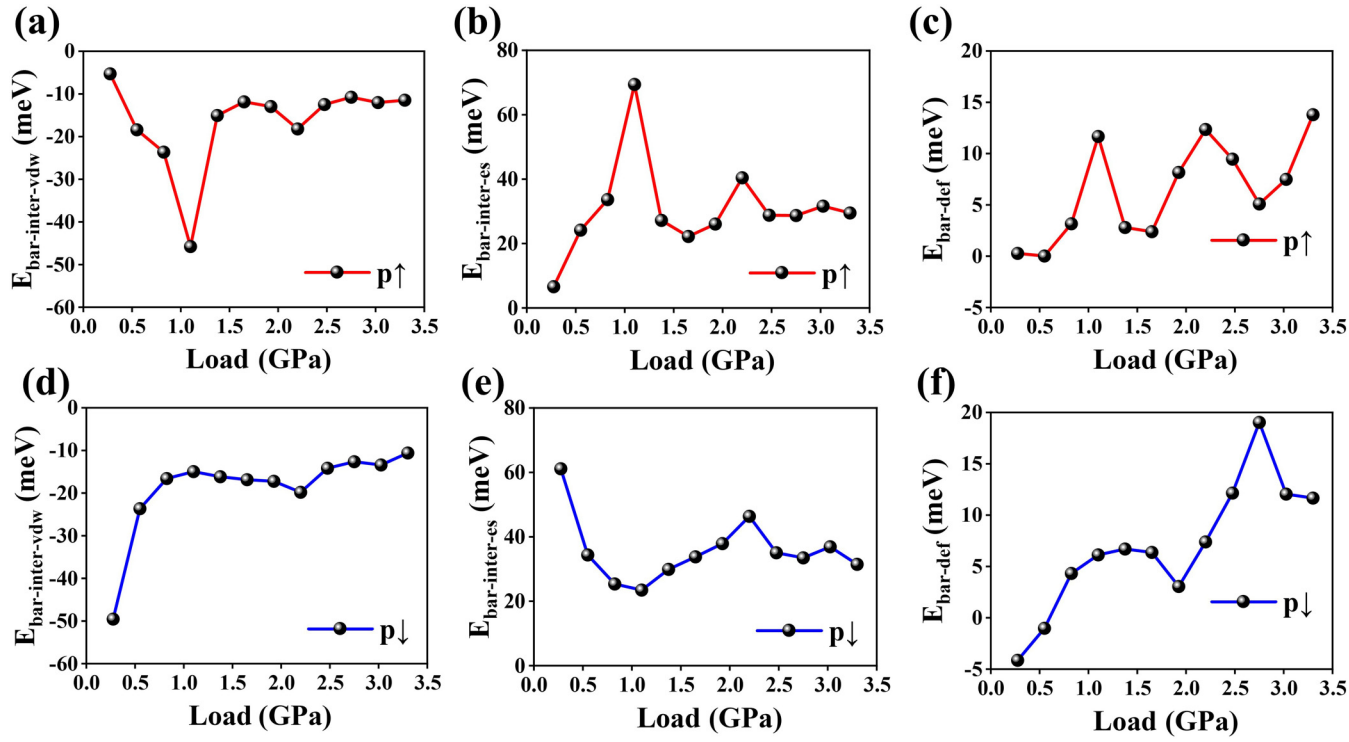

FIG. 3. Decomposed energy barriers (E_{bar}) for 1QL-In_2Se_3 sliding over graphene in two typical contacts. Contributed by (a) and (d) interlayer vdW interactions, $E_{bar-inter-vdW}$. (b) and (e) Interlayer electrostatic interactions, $E_{bar-inter-es}$. (c) and (f) Intralayer deformation energy of the 1QL-In_2Se_3 component, $E_{bar-def}$. (a)–(c) P ↑, (d)–(f) P ↓.

We also examined $E_{bar-inter}$ contributed, respectively, by the interlayer vdW interactions and the electrostatic interactions involving charge transfer, i.e., $E_{bar-inter-vdW}$ and $E_{bar-inter-es}$.

Specifically,

$$\begin{aligned} E_{bar-inter-vdW} &= [E_{max-vdW}(In_2Se_3 - graphene) - E_{max-vdW}(In_2Se_3) - E_{max-vdW}(graphene)] \\ &\quad - [E_{min-vdW}(In_2Se_3 - graphene) - E_{min-vdW}(In_2Se_3) - E_{min-vdW}(graphene)] \\ &= [E_{max-vdW}(In_2Se_3 - graphene) - E_{min-vdW}(In_2Se_3 - graphene)] - [E_{max-vdW}(In_2Se_3) - E_{min-vdW}(In_2Se_3)] \end{aligned} \tag{5}$$

and

$$E_{bar-inter-es} = E_{bar-inter} - E_{bar-inter-vdW}. \tag{6}$$

As shown in Fig. 3(a)–3(c), for the case of P ↑, we confirm that the delicate interplay among the three factors, i.e., $E_{bar-inter-vdW}$, $E_{bar-inter-es}$, and $E_{bar-def}$, result in the negative-positive oscillation of the differential friction coefficient μ. First, we found that, overall, the vdW interactions between In_2Se_3 and graphene contribute a negative value to E_{bar}, i.e., $E_{bar-iner-vdW} < 0$; however, both the interfacial electrostatic interactions and the intralayer deformation of 1QL-In_2Se_3 contribute positive values to E_{bar}, i.e., $E_{bar-inter-es}(E_{bar-def}) > 0$. Intriguingly, all three components of $E_{bar-iner-vdW}$, $E_{bar-inter-es}$, and $E_{bar-def}$ exhibit significant oscillations as the function of external load. However, the term $E_{bar-iner-vdW}$ possesses an out-of-phase oscillation toward the oscillation of E_{bar}, whereas both $E_{bar-iner-vdW}$ and $E_{bar-def}$ display in-phase oscillations compared to E_{bar}. Specifically, $E_{bar-iner-vdW}$ stands in the valley at 1.1 and 2.2 GPa [Fig. 3(a)], whereas both $E_{bar-iner-es}$ and $E_{bar-def}$, positioned on the peaks at the same load [Fig. 3(b) and 3(c)], exhibit the same feature as observed in the total E_{bar} shown in Fig. 2(c).

However, for the P ↓ contact, though overall E_{bar} monotonously increases within the load scope of 0 to 2.75 GPa, it begins to drop as the load increases up to around 2.40 and 2.75 GPa, corresponding to the feature of positive-to-negative transition of the friction coefficient μ. Similarly, as shown in Fig. 3(d)–3(f), the $E_{bar-iner-vdW}$ ($E_{bar-inter-es}$) term is negative (negative) to E_{bar}, and $E_{bar-def}$ is overall positive, except in the load regime of 0 to 0.55 GPa, in which a slight oscillation feature is observed. Moreover, the term $E_{bar-iner-vdW}$ also possesses out-of-phase oscillation relative to $E_{bar-inter-es}$, with the negative former being completely compensated by the positive latter, which leads to a net-positive E_{bar}. The positive $E_{bar-def}$ in the load regime of 0.55 to 2.75 GPa further enhances the monotonous increase of E_{bar}, whereas its substantial reduction beyond 2.75 GPa leads to

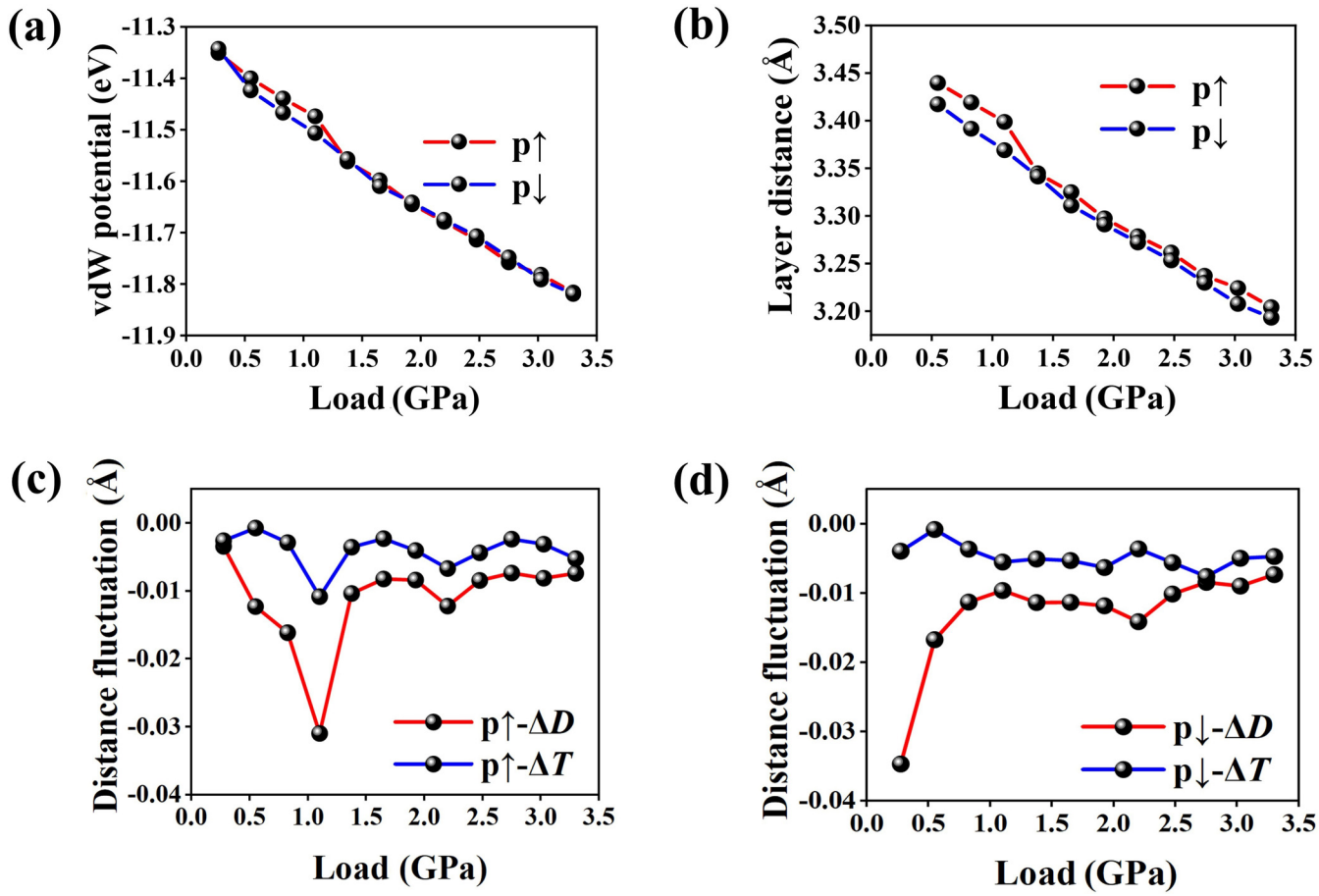

FIG. 4. Calculated parameters of the 1QL-In_2Se_3-raphene heterostructure for both P ↑ and P ↓ configurations under external load. (a) Energy profile of the vdW component and (b) interfacial distance D of the In_2Se_3-graphene heterostructure in the optimized E_{min} state. Variation of the differences of the interfacial distance (ΔD) and change of the thickness (ΔT) of the In_2Se_3 overlayer between the E_{max} and E_{min} states for (c) P ↑ and (d) P ↓.

the downward shift of the total E_{bar}, as shown in Fig. 2(d). Correspondingly, a significant positive-to-negative transition of the differential friction coefficient μ can be observed.

Now we illustrate the underlying mechanism of the negative contribution of the vdW term to E_{bar} with oscillations. As shown in Fig. 4, in the present load regime up to 3.3 GPa, the total energy of the vdW term monotonously decreases, subject to the external loading, which is also accompanied by the monotonous reduction of the interfacial distance (D). These results demonstrate that the vdW interactions lie in the attractive regime [42,43] beyond the equilibrium position of the In_2Se_3-graphene heterostructure due to the local interfacial charge repulsive interactions. Also importantly, it is found that, for a given load N, the interfacial distance D of the E_{max} state is uniformly smaller than that of E_{min} in the whole load regime; therefore, $E_{bar-inter-vdW}$ is negative in the attractive regime for both P ↑ and P ↓, as shown in Fig. 4(c) and (d). More specifically, for P ↑, the differences of the interfacial distance (ΔD) and the thickness (ΔT) between the E_{max} and E_{min} states exhibit a clear in-phase oscillation with $E_{bar-inter-vdW}$, as shown in Figs. 3(a) and 4(c), respectively. Correspondingly, upon the reduction of both ΔD and ΔT, for the P ↑ configuration, $E_{bar-inter-es}$ and $E_{bar-def}$ contribute positive values to E_{bar} with in-phase oscillation, mainly due to the repulsive interactions between the intrinsic dipole of 1QL-In_2Se_3 and the induced interfacial dipole, as schematically illustrated in Fig. 1(b). However, for P ↓, due to the attractive interactions of the intrinsic dipole and the induced interfacial dipole, ΔD and ΔT essentially exhibit out-of-phase oscillation, as shown in Fig. 4(d). Thus, $E_{bar-inter-es}$ and $E_{bar-def}$ balance each other, contributing to an overall net-positive E_{bar}.

To illustrate further the underlying physical mechanism of the intriguing oscillation of the interfacial sliding potential profile, taking the case of P ↑ under 1.1 GPa as a typical example, we perform electronic energy band analysis, upon which the origin of the variation of E_{bar} can be deduced. In doing this, we first present the energy band of the E_{min} state, as shown in Fig. 5(a), based on which we further show the variations of the energy band of the E_{max} state relative to that of E_{min}, as indicated by the deep-purple and deep-red regimes, where the energy band of the E_{max} states are downward- and upward-shifted, respectively, by 5 meV relative to the E_{min} states. Moreover, we select four representative energy states (I–IV) in the energy range of −1.2 to −0.5 eV at the high symmetry point, i.e., K, Γ, and M, to figure out the origin of E_{bar} by analyzing the electronic wavefunctions. From Fig. 5(a) and (b), one can see that all three states, i.e., I at the K-point,

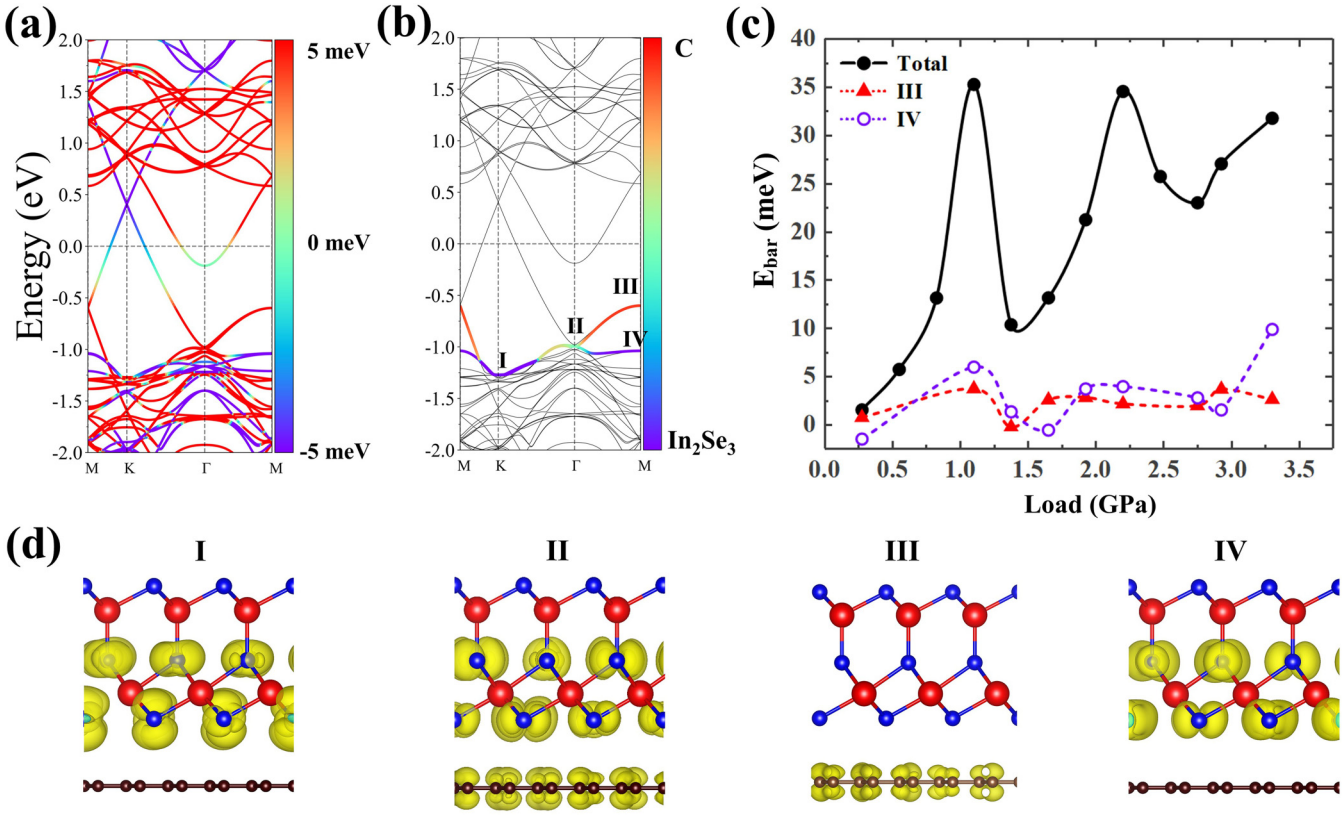

FIG. 5. Electronic structure analysis of the E_{min} and E_{max} states for the case of P↑ under 1.1 GPa. (a) Variation of the energy band structure of the E_{max} state relative to the E_{min} state, wherein the deep-purple and deep-red regimes imply that the energy band of the E_{max} state will be downward- and upward-shifted 5 meV relative to the E_{min} state as plotted. (b) Decomposed electronic band structure projected on substrate graphene (C) and In_2Se_3 overlayer. Four representative states (I–IV) at the high symmetry points (K, Γ, and M) are marked. (c) Total E_{bar} and that contributed by the III and IV states at the M-point. (d) Electronic charges of the four states, I to IV. The isosurface of the charge density is 0.005 e/Å^3.

II at the Γ-point, and III at the M-point, correspond to the positive contributions to E_{bar}, which are contributed primarily by In_2Se_3, a mixture of In_2Se_3 and graphene, and graphene, respectively. Importantly, as shown in Fig. 5(c), taking III and IV as typical examples, we find that E_{bar} contributed from these states possesses an overall in-phase oscillation with that of the total E_{bar}. Moreover, the contributions to E_{bar} of state III (mainly from graphene) and state IV (mainly from In_2Se_3) periodically cross over each other with an increasing external load N [see Fig. 5(c)]. In addition, all these three states possess a common feature that, at the interface, either the graphene or the In_2Se_3 component exhibits a p_z orbital characteristic, as demonstrated in Fig. 5(c). Particularly, for states II and III, the p_z states mainly contributed by graphene are relatively higher in energy compared to the In_2Se_3 component, which dominates the increase of E_{bar}. In contrast, for the IV state, which contributes negatively to E_{bar}, mainly by the In_2Se_3 component, only p_x- and p_y-dominant orbitals are identified. Moreover, in the vicinity of the K-point, the relatively low-energy states mainly originating from In_2Se_3 are also essentially p_x/p_y features that contribute to the downward shift of E_{bar}, which is in close agreement with our previous findings [61]. Given that the vdW interactions between 1QL-In_2Se_3 and graphene contribute a negative value to E_{bar} as analyzed, one can conclude the interlayer vdW interactions drive the p_x- and p_y-like energy levels downward in the E_{max} states, which dominate the negative friction. Moreover, with an increasing external load N, the competition between the vdW and electrostatic interactions result in a periodic shift of the p_x/p_y states relative to the p_z levels, which collectively leads to the oscillation of E_{bar} and the friction coefficient.

To illustrate further the underlying mechanism of the periodic oscillation in E_{bar} subject to the external loading, we further analyze the variations of the differential electronic charge density between the E_{max} and E_{min} states for both the valance band (VB) and the one right below the VB (VB-1) under 0 GPa, as shown in Fig. 6(a). First, one can see that, except at the Γ-point, the VB is mainly contributed by graphene, and the VB-1 originates from the hybridization of In_2Se_3 and graphene. Second, for the VB, the differential electronic charge density between the E_{max} and E_{min} states around the interface is considerably more significant at 1.1 GPa than that at 0.55 and 1.65 GPa, where the former corresponds to the maximum of E_{bar} and the latter to the minima, respectively. Moreover, at 2.2 GPa, the electronic charge density redistribution is further enhanced around the interface, and the second local maximum of E_{bar} occurs. These findings strongly suggest that it is the charge redistribution accompanied by the

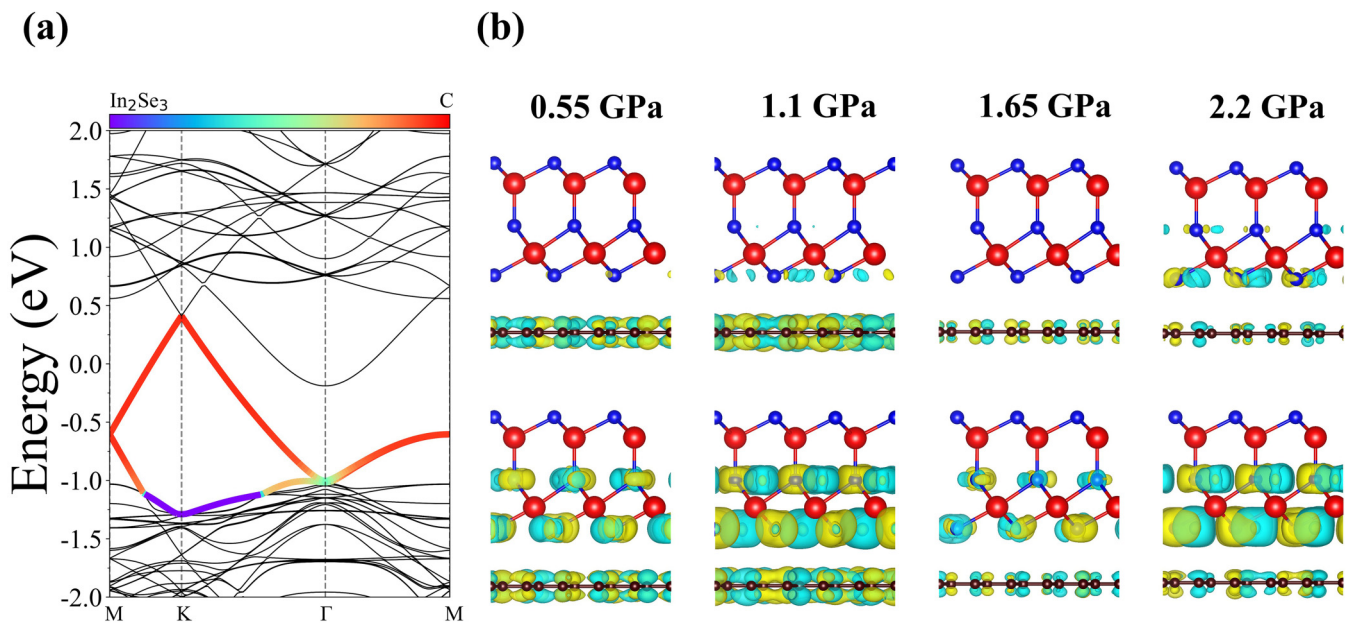

FIG. 6. Electronic structure analysis. (a) Decomposed band structure contributed by graphene and In_2Se_3 for the two representative energy bands around the Fermi level, i.e., valance band (VB) and VB-1 without external loading. (b) Variation of differential electronic charge density between the E_{max} and E_{min} states for both the VB presented in top panels and VB-1 in bottom panels, under $N = 0.55$, 1.1, 1.65, and 2.2 GPa. The isosurface of the charge density is 0.005 e/Å^3.

periodic crossover of the p_x/p_y and p_z states [Fig. 5(c)], and particularly the interfacial charge transfer between graphene and In_2Se_3 driven by the work of the external load, that leads to the total energy rise and thus results in the local maximum of E_{bar}.

Last, we note that the lattice mismatch between graphene and In_2Se_3 may lead to a spontaneous misalignment angle [62,63]. Such a misalignment angle may also lead to new physics on the friction [64,65], which will also be great interest to us in future investigations.

IV. CONCLUSION

In conclusion, with first-principles calculations, we predict that when sliding the ferroelectric two-dimensional (2D) In_2Se_3 over graphene, the differential friction coefficient μ, measured by the slope of the corrugation in the sliding potential energy barrier subject to an external load N, will display an overall positive feather when the dipole is aligned toward the In_2Se_3-graphene interface. However, μ exhibits an intriguing negative-positive oscillation with an increasing normal load when the dipole is aligned outward from the interface. That is, μ can be tuned on demand to be either negative or positive depending on the external load regime and the dipole alignments. Such a striking observation can be rationalized by the oscillation of the In_2Se_3-graphene interfacial charge accumulation driven by the intralayer charge redistribution of the 2D In_2Se_3 structure under an external load. Moreover, we reveal that the vdW interactions lead to a p_z orbital upward shift and account for the enhancement of the interfacial sliding friction, whereas the p_x- and p_y-like orbitals are downward-shifted, which dominate friction reduction and thus result in a negative differential friction coefficient. Moreover, with an increasing external load N, the periodic crossover of the p_x/p_y states relative to the p_z levels collectively leads to the oscillation of E_{bar} and the friction coefficient. The present findings are expected to stimulate delicate experimental verification, which may play an instrumental role in the design of high-performance solid lubricants and nanosensors.

ACKNOWLEDGMENTS

This work was supported by the NSF of China (Grants No. 12074345, No. 12174349, No. 11804306, and No. 12204421). The calculations were performed at the Supercomputer Center in Zhengzhou University (Zhengzhou), Zhengzhou University, Henan.

J.T.C. and K.L. contributed equally to this work.

[1] B. N. J. Persson, *Sliding Friction: Physical Principles and Applications* (Springer, Berlin, 2000).
[2] A. Vanossi, N. Manini, M. Urbakh, S. Zapperi, and E. Tosatti, Rev. Mod. Phys. **85**, 529 (2013).
[3] J. Xu and J. Li, Friction **3**, 344 (2015).
[4] D. Liu, X. Yin, H. Y. Guo, L. L. Zhou, X. Y. Li, C. L. Zhang, J. Wang, and Z. L. Wang, Sci. Adv. **5**, eaav6437 (2019).
[5] D. Berman, A. Erdemir, and A. V. Sumant, ACS Nano **12**, 2122 (2018).
[6] M. Urbakh, Nat. Nanotechnol. **8**, 893 (2013).
[7] K. Holmberg and A. Erdemir, Friction **5**, 263 (2017).
[8] D. Berman, S. A. Deshmukh, S. K. R. S. Sankaranarayanan, A. Erdemir, and A. V. Sumant, Science **348**, 1118 (2015).
[9] S. R. Saufi, Z. A. B. Ahmad, M. S. Leong, and M. H. Lim, IEEE Access **7**, 122644 (2019).

[10] O. M. Braun, I. Barel, and M. Urbakh, Phys. Rev. Lett. **103**, 194301 (2009).

[11] R. Sahli, G. Pallares, C. Ducottet, I. E. Ben Ali, S. Al Akhrass, M. Guibert, and J. Scheibert, Proc. Natl. Acad. Sci. USA **115**, 471 (2018).

[12] C. Androulidakis, E. N. Koukaras, G. Paterakis, G. Trakakis, and C. Galiotis, Nat. Commun. **11**, 1595 (2020).

[13] M. Urbakh, J. Klafter, D. Gourdon, and J. Israelachvili, Nature (London) **430**, 525 (2004).

[14] S. Achanta, T. Liskiewicz, D. Drees, and J. P. Celis, Tribol. Int. **42**, 1792 (2009).

[15] V. Bormuth, V. Varga, J. Howard, and E. Schaffer, Science **325**, 870 (2009).

[16] T. Guerin, J. Prost, P. Martin, and J. F. Joanny, Curr. Opin. Cell Biol. **22**, 14 (2010).

[17] Y. Braiman, J. Barhen, and V. Protopopescu, Phys. Rev. Lett. **90**, 094301 (2003).

[18] Z. Tshiprut, S. Zelner, and M. Urbakh, Phys. Rev. Lett. **102**, 136102 (2009).

[19] M. Evstigneev and P. Reimann, Phys. Rev. X **3**, 041020 (2013).

[20] E. Gnecco, R. Bennewitz, T. Gyalog, C. Loppacher, M. Bammerlin, E. Meyer, and H. J. Guntherodt, Phys. Rev. Lett. **84**, 1172 (2000).

[21] W. G. Ouyang, S. N. Ramakrishna, A. Rossi, M. Urbakh, N. D. Spencer, and A. Arcifa, Phys. Rev. Lett. **123**, 116102 (2019).

[22] P. A. Thoren, A. S. de Wijn, R. Borgani, D. Forchheimer, and D. B. Haviland, Nat. Commun. **7**, 13836 (2016).

[23] S. Li, Q. Li, R. W. Carpick, P. Gumbsch, X. Z. Liu, X. Ding, J. Sun, and J. Li, Nature (London) **539**, 541 (2016).

[24] C. Lee, Q. Y. Li, W. Kalb, X. Z. Liu, H. Berger, R. W. Carpick, and J. Hone, Science **328**, 76 (2010).

[25] T. Filleter, J. L. McChesney, A. Bostwick, E. Rotenberg, K. V. Emtsev, T. Seyller, K. Horn, and R. Bennewitz, Phys. Rev. Lett. **102**, 086102 (2009).

[26] H. T. Xie, S. L. Wang, and H. Huang, Tribol. Lett. **66**, 15 (2018).

[27] H. T. Xie, M. A. Ayoubi, W. S. Lu, J. D. Wang, J. B. Huang, and W. Wang, Sci. Rep. **7**, 8459 (2017).

[28] D. Andersson and A. S. de Wijn, Nat. Commun. **11**, 420 (2020).

[29] M. H. Müser, Europhys. Lett. **66**, 97 (2004).

[30] K. Shinjo and M. Hirano, Surf. Sci. **283**, 473 (1993).

[31] Y. N. Zhang, F. Hanke, V. Bortolani, M. Persson, and R. Q. Wu, Phys. Rev. Lett. **106**, 236103 (2011).

[32] W. Gao and A. Tkatchenko, Phys. Rev. Lett. **114**, 096101 (2015).

[33] M. R. Y. Vazirisereshk, H. Ye, Z. J. Otero-de-la-Roza, A. Zhao, M. Q. Gao, Z. L. Johnson, A. T. C. Johnson, E. R. Carpick, and R. W. Martini, Nano Lett. **19**, 5496 (2019).

[34] M. Peyrard and S. Aubry, J. Phys. C Solid State Phys. **16**, 1593 (1983).

[35] M. Hirano, K. Shinjo, R. Kaneko, and Y. Murata, Phys. Rev. Lett. **67**, 2642 (1991).

[36] Z. Deng, A. Smolyanitsky, Q. Li, X. Q. Feng, and R. J. Cannara, Nat. Mater. **11**, 1032 (2012).

[37] B. T. W. Liu, J. Zhao, S. J. Qu, C. Y. Liu, Y. Ma, L. R. Zhang, Z. H. Liu, K. H. Zheng, and Q. S. Ma, Sci. Adv. **6**, eaaz6787 (2020).

[38] P. Monceau, J. Richard, and M. Renard, Phys. Rev. B **25**, 931 (1982).

[39] L. Chen, Z. P. Hu, A. D. Zhao, B. Wang, Y. Luo, J. L. Yang, and J. G. Hou, Phys. Rev. Lett. **99**, 146803 (2007).

[40] Y. Song, D. Mandelli, O. Hod, M. Urbakh, M. Ma, and Q. Zheng, Nat. Mater. **17**, 894 (2018).

[41] M. Dienwiebel, G. S. Verhoeven, N. Pradeep, J. W. M. Frenken, J. A. Heimberg, and H. W. Zandbergen, Phys. Rev. Lett. **92**, 126101 (2004).

[42] J. H. Sun, Y. Y. Lu, Y. Q. Feng, Z. B. Lu, G. A. Zhang, Y. P. Yuan, L. M. Qian, and Q. J. Xue, Tribol. Lett. **68**, 18 (2020).

[43] C. B. Yang, S. Y. Xiao, J. C. Yang, X. M. Lu, Y. H. Chu, M. Zhou, F. Z. Huang, and J. S. Zhu, Appl. Surf. Sci. **457**, 797 (2018).

[44] C. R. Woods, F. Withers, M. J. Zhu, Y. Cao, G. Yu, A. Kozikov, M. Ben Shalom, S. V. Morozov, M. M. van Wijk, A. Fasolino, M. I. Katsnelson, K. Watanabe, T. Taniguchi, A. K. Geim, A. Mishchenko, and K. S. Novoselov, Nat. Commun. **7**, 10800 (2016).

[45] A. Smolyanitsky and J. P. Killgore, Phys. Rev. B **86**, 125432 (2012).

[46] A. Smolyanitsky, RSC Adv. **5**, 29179 (2015).

[47] Y. Zhang, M. Dong, B. Gueye, Z. H. Ni, Y. J. Wang, and Y. F. Chen, Appl. Phys. Lett. **107**, 011601 (2015).

[48] J. Xiao, H. Zhu, Y. Wang, W. Feng, Y. Hu, A. Dasgupta, Y. Han, Y. Wang, D. A. Muller, L. W. Martin, P. A. Hu, and X. Zhang, Phys. Rev. Lett. **120**, 227601 (2018).

[49] J. Sun, L. Zhang, R. Pang, X. J. Zhao, J. Cheng, Y. Zhang, X. Xue, X. Ren, W. Zhu, S. Li, and Z. Zhang, Adv. Sci. **9**, 2103443 (2022).

[50] P. Hohenberg and W. Kohn, Phys. Rev. **136**, B864 (1964).

[51] G. Kresse and J. Furthmuller, Phys. Rev. B **54**, 11169 (1996).

[52] P. E. Blochl, Phys. Rev. B **50**, 17953 (1994).

[53] J. P. Perdew, K. Burke, and M. Ernzerhof, Phys. Rev. Lett. **77**, 3865 (1996).

[54] S. Grimme, J. Antony, S. Ehrlich, and H. Krieg, J. Chem. Phys. **132**, 154104 (2010).

[55] W. Ding, J. Zhu, Z. Wang, Y. Gao, D. Xiao, Y. Gu, Z. Zhang, and W. Zhu, Nat. Commun. **8**, 14956 (2017).

[56] J. H. Sun, Y. N. Zhang, Z. B. Lu, Q. Y. Li, Q. J. Xue, S. Y. Du, J. B. Pu, and L. P. Wang, J. Phys. Chem. Lett. **9**, 2554 (2018).

[57] C. Cui, W.- J. Hu, X. Yan, C. Addiego, W. Gao, Y. Wang, Z. Wang, L. Li, Y. Cheng, and P. Li, Nano Lett. **18**, 1253 (2018).

[58] Y. Zhou, D. Wu, Y. Zhu, Y. Cho, Q. He, X. Yang, K. Herrera, Z. Chu, Y. Han, M. C. Downer, H. Peng, and K. Lai, Nano Lett. **17**, 5508 (2017).

[59] J. Zhou, Q. Zeng, D. Lv, L. Sun, L. Niu, W. Fu, F. Liu, Z. Shen, C. Jin, and Z. Liu, Nano Lett. **15**, 6400 (2015).

[60] L. L. Kang, P. Jiang, H. Hao, Y. H. Zhou, X. H. Zheng, L. Zhang, and Z. Zeng, Phys. Rev. B **101**, 014105 (2020).

[61] K. Liu, J. Cheng, X. Zhao, Y. Zhu, X. Ren, J. Shi, Z. Guo, C. Shan, H. Liu, and S. Li, Nano Res. **15**, 5758 (2022).

[62] A. D. Novaco and J. P. McTague, Phys. Rev. Lett. **38**, 1286 (1977).

[63] J. P. McTague and A. D. Novaco, Phys. Rev. B **19**, 5299 (1979).

[64] D. Mandelli, A. Vanossi, N. Manini, and E. Tosatti, Phys. Rev. Lett. **114**, 108302 (2015).

[65] R. Guerra, M. van Wijk, A. Vanossi, A. Fasolino, and E. Tosatti, Nanoscale **9**, 8799 (2017).